

Backend-agnostic Julia framework for 3D modeling and inversion of gravity data

Nimatullah^a, Pankaj K Mishra^b, Jochen Kamm^b and Anand Singh^a

^aDepartment of Earth Sciences, Indian Institute of Technology, Bombay, India

^bGeological Survey of Finland

ARTICLE INFO

Keywords:

Gravity inversion
GPU acceleration
High-performance computing
Julia programming
Data-space inversion

ABSTRACT

This paper presents a high-performance framework for three-dimensional gravity modeling and inversion implemented in Julia, addressing key challenges in geophysical modeling such as computational complexity, ill-posedness, and the non-uniqueness inherent to gravity inversion. The framework adopts a data-space inversion formulation to reduce the dimensionality of the problem, leading to significantly lower memory requirements and improved computational efficiency while maintaining inversion accuracy. Forward modeling and inversion operators are implemented within a backend-agnostic kernel abstraction, enabling execution on both multicore CPUs and GPU accelerators from a single code base. Performance analyses conducted on NVIDIA CUDA GPUs demonstrate substantial reductions in runtime relative to CPU execution, particularly for large-scale datasets involving up to approximately 3.3 million rectangular prisms, highlighting the scalability of the proposed approach. The inversion incorporates implicit model constraints through the data-space formulation and depth-weighted sensitivity, which mitigate depth-related amplitude decay and yield geologically coherent, high-resolution subsurface density models. Validation using synthetic models confirms the ability of the framework to accurately reconstruct complex subsurface structures such as vertical and dipping dykes. Application to field gravity data further demonstrates the robustness and practical utility of the GPU-accelerated framework, with the recovered models showing strong consistency with independent geological constraints and prior interpretations. Overall, this work underscores the potential of GPU-enabled computing in Julia to transform large-scale gravity inversion workflows, providing an efficient, extensible, and accurate computational solution for high-resolution geophysical studies.

1. Introduction

Three-dimensional (3D) gravity inversion is a powerful geophysical technique to infer subsurface density distributions from gravity anomaly data. This method is widely applied in resource exploration, geodynamic studies, and environmental investigations to model geological structures such as ore bodies, sedimentary basins, and crustal heterogeneities (Tirel et al., 2004; Jacoby and Smilde, 2009; Reynolds, 2011; Singh, 2019) and is important first-step towards a lithospheric digital twin (Mishra, 2025). By converting observed gravity anomalies into a 3D density distribution, inversion techniques provide critical insights into subsurface properties without requiring direct drilling or intrusive measurements. However, 3D gravity inversion is inherently non-unique, as gravity observations alone are insufficient to uniquely determine the underlying density distribution. Multiple subsurface models can reproduce the same gravity response. Furthermore, the presence of noise, limited data coverage, and model discretization renders the inversion problem ill-posed, necessitating the use of regularization to obtain stable and physically meaningful solutions. (Li and Oldenburg, 1998; Camacho et al., 2000, 2002; Rim et al., 2007; Gottsmann et al., 2008). Researchers have developed

various inversion algorithms to address this issue, often incorporating regularization techniques to stabilize the solution and reduce ambiguities. One of the most widely used methods is L_2 -norm regularization, which enforces smoothness constraints to prevent unrealistic density variations in the solution (Oldenburg and Li, 1994; Li and Oldenburg, 1998; Hightower et al., 2020).

Despite its effectiveness, L_2 -norm regularization has notable limitations. It tends to smooth out sharp density contrasts, which can obscure critical geological features such as ore bodies, fault zones, or lithological boundaries. To overcome this, alternative approaches have been explored, including L_1 norm and sparsity-promoting regularization techniques, which improve resolution by preserving sharp edges in the reconstructed density model (Jafarpour et al., 2009; Utsugi, 2019; Meng, 2018). While such approaches can enhance edge preservation, the present study focuses on a computationally efficient quadratic data-space inversion framework, emphasizing scalability and performance rather than sparsity-promoting regularization.

In addition, joint inversion algorithms that integrate gravity data with complementary geophysical datasets, such as seismic, magnetic, or electrical resistivity data, have been developed to improve resolution and reduce uncertainty in subsurface models (Carrillo and Gallardo, 2018; Lelièvre et al., 2012; Moorkamp et al., 2011; Fregoso and Gallardo, 2009). Incorporating geological constraints, such as well log data, lithological boundaries, and previous geological knowledge, further refines the results of inversion and improves interpretability (Bosch and McGaughey, 2001; Calcagno et al., 2008).

Another major challenge in 3D gravity inversion is computational complexity, especially when dealing with large-scale datasets. Traditional CPU-based implementations can become computationally prohibitive in terms of runtime and memory consumption, particularly when working with models involving tens or hundreds of millions of unknowns.

In response to these computational challenges, this study presents a high-performance 3D gravity inversion framework implemented in Julia, a modern programming language designed for high-performance scientific computing (Bezanson et al., 2017; Jones et al., 2020). The framework leverages data space inversion to reduce the dimensionality of the problem, thereby improving computational efficiency while maintaining inversion accuracy (Rezaie et al., 2017; Marchetti et al., 2014).

The framework is designed to support both CPU and vendor-neutral GPU execution. GPU acceleration is implemented and benchmarked on NVIDIA CUDA GPUs, significantly enhances computational performance by parallelizing large-scale linear algebra operations and reducing data transfer bottlenecks. Benchmarking results show that GPU-based execution leads to substantial reductions in runtime compared to CPU-based computations, especially for large-scale problems involving models with up to approximately 3.3 million rectangular prisms. The framework retains numerical accuracy and stability across both architectures, making it suitable for large-scale inversion using standard as well as physics-based machine learning method (Mishra et al., 2025) through accelerated and differentiable forward solver.

This paper evaluates the proposed GPU-accelerated 3D gravity inversion framework through a series of synthetic and field-based examples. The synthetic tests confirm the method's ability to resolve complex subsurface structures such as dipping and vertical dykes, while the field application validates the robustness and geological consistency of the inversion results. Overall, this work highlights the potential of GPU-enabled computing to transform large-scale geophysical modeling, providing a scalable and efficient alternative for subsurface imaging.

2. Methodology

2.1. 3D Gravity Forward Modeling

The gravitational response of subsurface structures is computed using a vertex-centered approach. For a rectangular prism defined by vertices (x_p, y_q, z_r) where $p, q, r \in \{1, 2\}$, the vertical gravity component at the observation point $(0, 0, 0)$ is given by (Blakely, 1996):

$$g_z = G\rho \sum_{p=1}^2 \sum_{q=1}^2 \sum_{r=1}^2 \sigma_{pqr} \Psi(x_p, y_q, z_r) \quad (1)$$

where $\sigma_{pqr} = (-1)^{p+q+r}$ is the vertex parity operator, and $\Psi(x, y, z)$ is defined as:

$$\Psi(x, y, z) = z \tan^{-1} \left(\frac{xy}{z\mathcal{R}} \right) - x \ln(\mathcal{R} + y) - y \ln(\mathcal{R} + x), \quad (2)$$

with:

$$\mathcal{R} = \sqrt{x^2 + y^2 + z^2}. \quad (3)$$

2.2. 3D Gravity Inversion

The subsurface density distribution is estimated by minimizing the objective function:

$$\min_{\mathbf{m}} \phi(\mathbf{m}) = (\mathbf{d}^{\text{obs}} - \mathbf{C}\mathbf{m})^T \mathbf{W}_d^{-1} (\mathbf{d}^{\text{obs}} - \mathbf{C}\mathbf{m}) + (\mathbf{m} - \mathbf{m}_{\text{ref}})^T \mathbf{W}_m^{-1} (\mathbf{m} - \mathbf{m}_{\text{ref}}) \quad (4)$$

In this formulation, \mathbf{d}^{obs} is the observed gravity anomaly vector ($N \times 1$), \mathbf{C} is the forward modeling matrix ($N \times M$), \mathbf{m} is the density parameter vector ($M \times 1$), \mathbf{m}_{ref} is the reference model ($M \times 1$), \mathbf{W}_d and \mathbf{W}_m are the data weighting matrix and regularization matrix ($N \times N$ and $M \times M$, respectively)

Differentiating with respect to \mathbf{m} yields the linear system:

$$(\mathbf{C}^T \mathbf{W}_d^{-1} \mathbf{C} + \mathbf{W}_m^{-1}) (\mathbf{m} - \mathbf{m}_{\text{ref}}) = \mathbf{C}^T \mathbf{W}_d^{-1} (\mathbf{d}^{\text{obs}} - \mathbf{C}\mathbf{m}_{\text{ref}}) \quad (5)$$

Direct inversion of (5) is computationally prohibitive for $M \sim 10^5\text{--}10^6$.

Using the matrix identity (Wang et al., 2015):

$$(\mathbf{C}^T \mathbf{W}_d^{-1} \mathbf{C} + \mathbf{W}_m^{-1})^{-1} \mathbf{C}^T \mathbf{W}_d^{-1} = \mathbf{W}_m \mathbf{C}^T (\mathbf{C} \mathbf{W}_m \mathbf{C}^T + \mathbf{W}_d)^{-1} \quad (6)$$

Using a matrix identity, we rewrite it as:

$$\delta\mathbf{m} = \mathbf{W}_m \mathbf{C}^T (\mathbf{C} \mathbf{W}_m \mathbf{C}^T + \mathbf{W}_d)^{-1} (\mathbf{d}^{\text{obs}} - \mathbf{C}\mathbf{m}_{\text{ref}}) \quad (7)$$

where $\delta\mathbf{d} = \mathbf{d}^{\text{obs}} - \mathbf{C}\mathbf{m}_{\text{ref}}$.

The solution becomes:

$$\delta\mathbf{m} = \mathbf{W}_m \mathbf{C}^T (\mathbf{C} \mathbf{W}_m \mathbf{C}^T + \mathbf{W}_d)^{-1} \delta\mathbf{d} \quad (8)$$

where $\delta\mathbf{m} = \mathbf{m} - \mathbf{m}_{\text{ref}}$ and $\delta\mathbf{d} = \mathbf{d}^{\text{obs}} - \mathbf{C}\mathbf{m}_{\text{ref}}$. This reduces the system size to $N \times N$ ($N \ll M$).

In gravity inversion studies, the construction of the sensitivity matrix (\mathbf{C} , also referred to as the G-matrix) and the subsequent inversion process are computationally demanding tasks, particularly for large-scale 3D problems. To address these challenges, a data-space inversion approach is employed, which significantly reduces computational time by operating on a reduced system size. This method leverages the efficiency of working in the data domain rather than directly solving the full model space, making it especially suitable for large datasets. Data-space inversion formulations have been shown to significantly reduce the computational burden of large-scale gravity inversion by operating on systems defined in the data domain rather than the full model space (Oldenburg and Li, 1994; Pilkington, 2009).

To further accelerate computations, especially for large-scale problems, we compare the performance of our inversion code executed on a central processing unit (CPU) and a graphics processing unit (GPU). Both implementations utilize the same numerical algorithm and data but differ in computational architecture. The GPU version leverages parallel

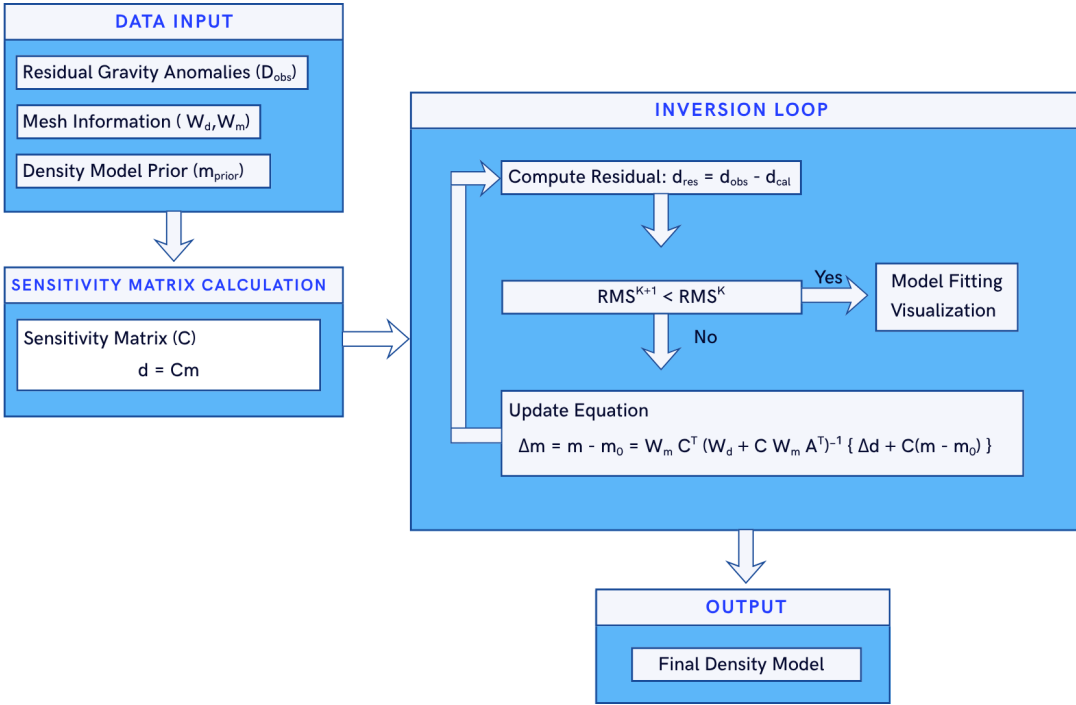


Figure 1: Computational workflow of the 3D gravity inversion framework

processing to perform matrix operations, particularly matrix multiplications and factorizations, more efficiently than the CPU.

The GPU acceleration methodology employs a multifaceted parallelization strategy to overcome computational bottlenecks in 3D gravity inversion. Backend-agnostic GPU kernels, executed on the CUDA backend, distribute gravitational response calculations across thousands of GPU threads, with each thread handling specific observation-cell pairs using singularity-robust formulations. Optimization of the memory hierarchy strategically places data across global memory (sensitivity matrix), shared memory (cell parameters), constant memory (physical constants), and register storage (intermediate results) to maximize throughput.

3. Backend-agnostic kernel abstraction

The parallel implementation in this work is based on `KernelAbstractions.jl`, which provides a hardware-agnostic abstraction for writing GPU-style kernels in Julia. Kernels are defined once using an abstract execution model and can be executed on different compute backends by changing only the backend selection at runtime. As a result, the same kernel code can run on multi-core CPUs or GPUs without modification. This approach differs from conventional GPU acceleration strategies, where separate device-specific forward kernels are typically required for CPU and GPU execution. In `KernelAbstractions.jl`, backend-specific details such as thread organization, indexing, and memory execution are handled internally, allowing the kernel logic to remain independent of the target hardware. Kernels developed and validated on the CPU can therefore be executed directly on the GPU using the same source code. In addition to CPU-GPU portability, kernel abstraction enables cross-vendor GPU portability. The same kernel formulation can, in principle, be executed on different GPU architectures, including NVIDIA (CUDA), AMD, and Apple Metal backends. Although performance results in this study are reported only for the CUDA backend, the kernel implementations themselves are backend-agnostic.

```

1 using KernelAbstractions
2 using CUDA
3
4 # Backend selection:
5 # Replace CUDABackend() with CPU(), AMDGPUBackend(), or MetalBackend()
6 # to run the same kernel on different hardware.
7 backend = CUDA.CUDABackend()
8
9 @kernel function scale_kernel!(A)
10    i = @index(Global)
11    if i <= length(A)
12        A[i] = 2.0f0 * A[i]
13    end
14 end
15
16 A = KernelAbstractions.ones(backend, Float32, 1024)
17 scale_kernel!(backend)(A; ndrange = length(A))
18 KernelAbstractions.synchronize(backend)

```

Backend-agnostic GPU kernel implementation using KernelAbstractions.jl

4. Results and Discussion

4.1. Computational Performance Comparison in Gravity Inversion

Figure 2 shows the computational cost associated with the construction of the gravity sensitivity matrix as a function of model size for both CPU and GPU implementations. For models with a small number of rectangular prisms, the CPU performs slightly faster than the GPU because GPU execution involves kernel initialization and host–device data transfer overheads that dominate total runtime when the computational workload is small. In contrast, CPUs are optimized for low-latency serial operations and can therefore handle small problem sizes efficiently without significant parallelization overhead. As a result, for models with fewer than approximately 10^3 cells, the benefits of GPU parallelism do not fully amortize the associated overhead costs.

As the model size increases, the computational characteristics change fundamentally. Beyond approximately 10^3 – 10^4 rectangular prisms, the arithmetic workload becomes sufficiently large for the GPU to exploit its massively parallel architecture. The CPU runtime increases rapidly with problem size, while the GPU runtime increases much more slowly with problem size and remains relatively stable over several orders of magnitude. For large-scale models exceeding 10^5 cells and extending up to about 3.3×10^6 rectangular prisms, CPU computation times surpass 10^3 seconds, whereas the GPU performs the same computation in approximately 20–30 seconds, yielding one to two orders of magnitude speedup. For problem sizes larger than approximately 3.3×10^6 prisms, the computation could not be completed on the Mahti GPU system due to a memory error.

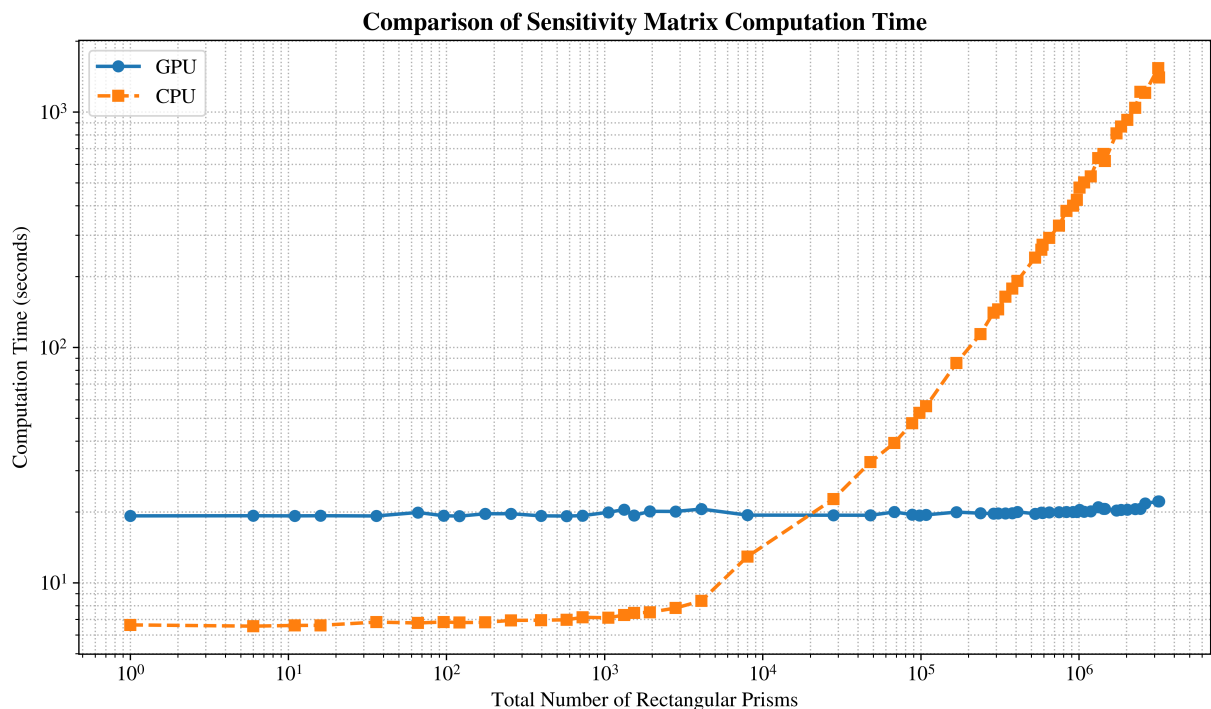


Figure 2: Log-log plot comparing computation time for sensitivity matrix construction using GPU versus CPU implementations across varying total number of cells. The GPU demonstrates dramatically better scaling, achieving significant speedup for large-scale models up to 3.3×10^6 cells, making GPU acceleration essential for practical 3D gravity inversion workflows.

4.2. Synthetic Example 1

The first synthetic experiment was designed to evaluate the capability of the proposed data space inversion framework to recover multiple isolated density anomalies with different lateral positions and depth extents. Two rectangular prismatic bodies embedded in a homogeneous background were considered to provide a controlled validation scenario.

The true density model is shown in Figure 3(a,c). Both bodies were assigned a density contrast of 1.0 g/cm^3 relative to the background, whose density was set to 0 g/cm^3 . Target 1 extends from 1,000 m to 4,000 m in the x -direction and from 1,000 m to 5,000 m in the y -direction, occupying depths between 2,000 m and 6,000 m. Target 2 is positioned farther east, spanning 8,000–12,000 m in both the x - and y -directions and extending from 4,000 m to 6,000 m depth. This configuration introduces spatial separation and depth variation, enabling an assessment of the inversion's resolving capability.

Synthetic gravity data were generated from the true model using the forward modeling operator and subsequently inverted using the data space inversion approach. No a priori constraints on the geometry or number of bodies were imposed during the inversion.

The inverted density models are shown in Figure 3(b,d). The isosurface representation highlights the recovered geometry of the anomalous bodies, allowing a direct comparison with the true model independent of density magnitude. The slice view further illustrates that both targets are reconstructed with accurate lateral extent and depth range. Minor smoothing is observed near the body boundaries, which is expected due to the non-uniqueness of gravity data and the applied regularization.

Overall, these results demonstrate that the data space inversion approach can effectively resolve multiple subsurface density anomalies and reliably recover their geometry and spatial distribution under idealized conditions.

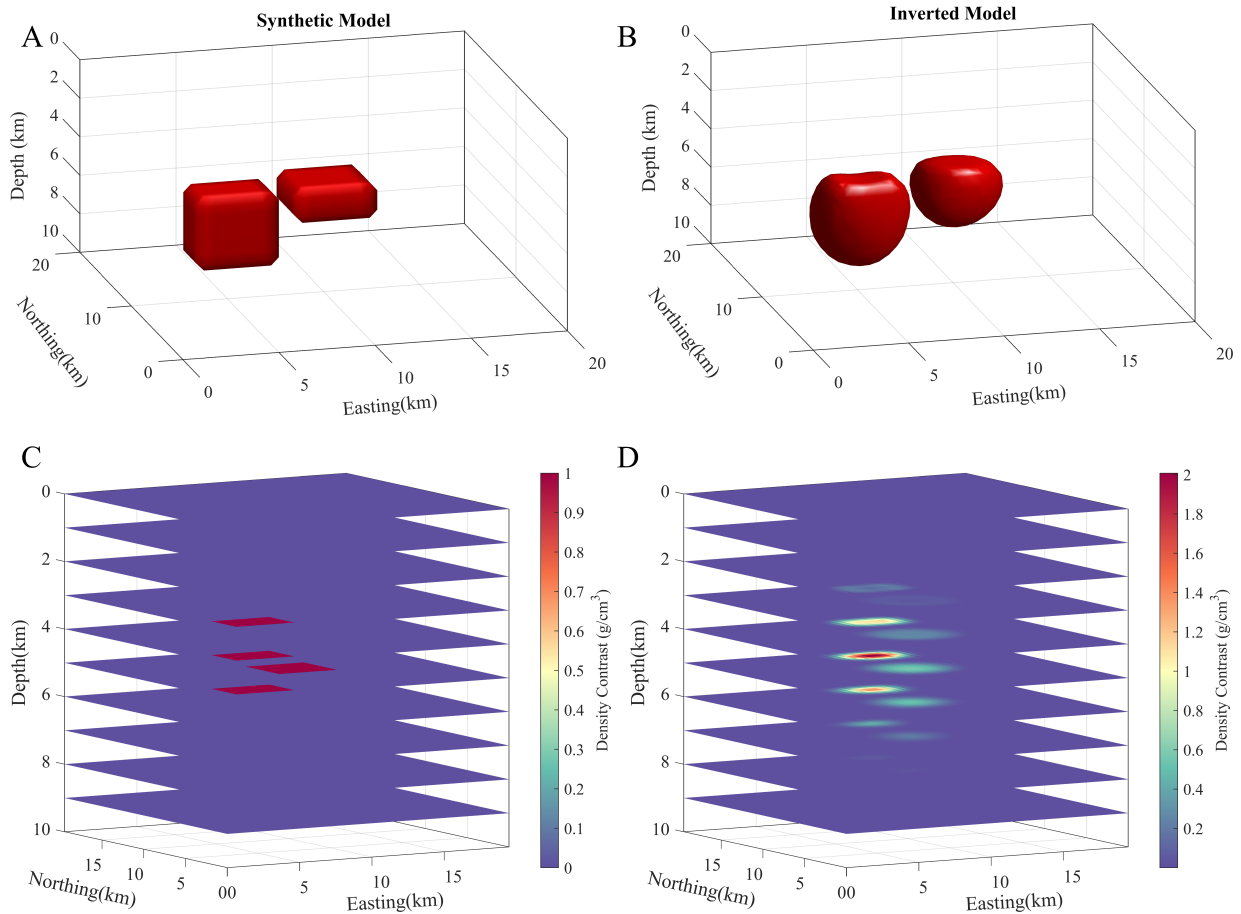


Figure 3: Combined visualization of the synthetic model and inversion results. (a) Synthetic density model displayed using an isosurface representation. (b) Inverted density model visualized with isosurfaces for comparison with the true geometry. (c) Slice view of the synthetic model showing the internal density distribution. (d) Slice view of the inverted model illustrating the recovered subsurface structure. Together, the panels provide a direct comparison between the true density distribution and the inversion output, demonstrating the ability of the method to recover both the geometry and internal characteristics of the anomalous bodies.

4.3. Synthetic Example 2

The second synthetic experiment was designed to assess the robustness of the data space inversion framework in resolving structurally complex subsurface features. A single dipping dyke was considered, representing a more realistic geological scenario involving inclined density contrasts.

The true density model is shown in Figure 4(a,c). The dyke exhibits a density contrast of 1.0 g/cm^3 relative to the homogeneous background and extends from depths of 3,000 m to 7,000 m. Laterally, the structure spans 8,000–12,000 m in the north direction and 5,000–12,000 m in the east direction. The background density was set to 0 g/cm^3 . This model introduces geometric complexity through its dip, depth extent, and lateral continuity, providing a stringent test for the inversion methodology.

Synthetic gravity data were computed from the true model and inverted using the data space inversion approach without incorporating prior information regarding the dyke geometry or orientation.

The inversion results are shown in Figure 4(b,d). The isosurface visualization reveals that the dipping geometry of the dyke is accurately recovered, allowing clear identification of its orientation and spatial extent. The slice view of the inverted model confirms that the inversion captures the primary subsurface characteristics, including the dip, depth range, and lateral continuity of the structure. Minor smoothing is present near the edges of the anomaly, consistent with the inherent resolution limitations of gravity data.

These results confirm that the data space inversion framework is capable of resolving dipping density structures and geometrically complex anomalies, supporting its applicability to realistic gravity-based subsurface investigations.

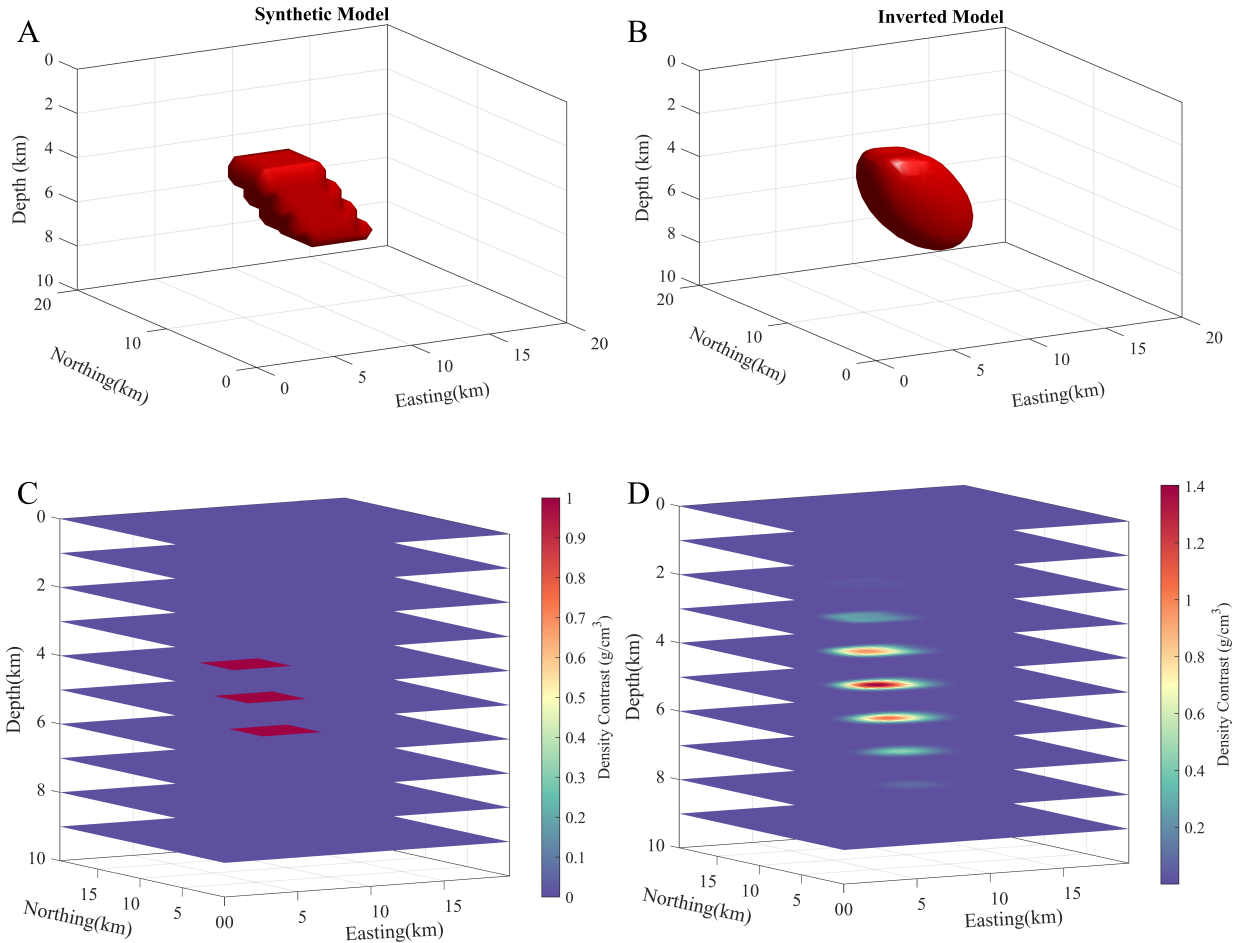


Figure 4: Combined visualization of the synthetic model and inversion results for the dipping dyke example. (a) Isosurface representation of the synthetic density model. (b) Isosurface visualization of the inverted model showing the recovered dyke geometry. (c) Slice view of the synthetic model illustrating internal density structure. (d) Slice view of the reconstructed density model obtained using data space inversion. Together, the panels provide a comprehensive comparison between the true model and the inversion output, demonstrating the ability of the method to resolve dipping subsurface structures.

4.4. Field Data -1: Geology of the Study Area

To assess the effectiveness of the proposed Julia-based 3D gravity inversion framework, we applied it to real-world field data from Tangarparha, Odisha, India—a site previously investigated by [Mohanty et al. \(2011\)](#) for chromite exploration. Their study integrated geological and geophysical observations to characterize a 5 km^2 area comprising several lithological units, including sheared granite, quartzofeldspathic gneiss, and mafic/ultramafic rocks (Figure 5). Gravity anomalies within this region are attributed to tectonically deformed and metamorphosed ultramafic bodies, which act as key indicators of subsurface geological structures.

The reliability of our inversion framework was evaluated by comparing the computed gravity response with the observed field data (Figure 6). The close agreement between the two datasets indicates that the inversion successfully captures the major subsurface density variations. These findings are consistent with previous geological interpretations suggesting that the region is dominated by quartzofeldspathic gneiss and sheared granite, which serve as host rocks for intrusive mafic/ultramafic bodies. The intrusions include hypabyssal dykes and coarse-grained plutonic units exhibiting cumulate textures, indicative of crystallization within a magma chamber. Chromite mineralization in the area is attributed to magma mixing and crustal assimilation processes within these ultramafic units.

To investigate the internal structure of the subsurface in greater detail, depth-wise vertical cross-sections were extracted from the recovered density model (Figure 7). These slices, spanning depths of 50–300 m, reveal a persistent high-density anomaly that extends vertically through multiple levels. This continuity supports the presence of a substantial mafic/ultramafic intrusion. Moreover, the variation in the anomaly's shape and magnitude with depth provides important constraints on the geometry, thickness, and orientation of the intrusive body, further supporting its association with chromite mineralization in the region.

A combined visualization of the inversion output, including both a density slice and a 3D isosurface representation, is shown in Figure 8. The slice offers a depth-resolved view of the density contrast distribution, highlighting localized high-density zones corresponding to the ultramafic intrusion. The accompanying 3D isosurface model delineates the geometry, lateral continuity, and spatial extent of the dense body. Together, these visualizations provide a comprehensive interpretation of both the internal density structure and the overall morphology responsible for the observed gravity anomalies.

4.5. Field Data -2: Geology of the Study Area

The study area is characterized by a pronounced gravity high, indicating the presence of dense subsurface formations. Field surveys and laboratory analysis of rock samples reveal a wide range of lithologies, with banded iron formations (BIF) exhibiting the highest measured density (3.746 g/cm^3) and sandstone the lowest (2.5 g/cm^3). The Bouguer anomaly map further highlights significant lateral and vertical variations in gravity response, suggesting a heterogeneous subsurface architecture.

Geologically, the area is located in the southeastern part of Bharatpur District and lies along the Great Boundary Fault zone, marking the transition between the Vindhyan Basin and the Delhi Supergroup. The lithological sequence includes formations of the Bhander Group (Vindhyan Supergroup), dominated by sandstones and shales, and older rocks of the Alwar and Ranthambhore Groups (Delhi Supergroup), composed primarily of quartzites and phyllites. In several locations, these units are overlain by Quaternary alluvium. The region is structurally complex, with both regional and local faults contributing to the observed gravity variations and influencing subsurface density distributions.

The gravity survey integrates measurements collected along access roads, cart tracks, canal corridors, and footpaths, ensuring broad spatial coverage. Density measurements from field samples confirm considerable variability, reflecting the mixture of sedimentary and metamorphic lithologies within the region. Elevation corrections using differential GPS (DGPS) further refine the dataset, supporting the interpretation of structural controls likely associated with tectonic movements along the Great Boundary Fault. The geological characterization is based on information compiled from [Singh \(2019\)](#).

Figure 9 presents the geological map of the study region, outlining the major lithological units and structural elements. Figure 10 shows the comparison between observed and computed residual gravity anomalies, illustrating the consistency of the inversion model with field measurements.

The recovered 3D density structure is visualized through a combined slice and isosurface representation (Figure 11). The slice sections reveal pronounced lateral and vertical heterogeneity, with high-density zones—shown in red—corresponding to BIF and other dense geological units that agree with mapped lithologies. The accompanying isosurface visualization captures the three-dimensional geometry, continuity, and orientation of these dense bodies. The structures exhibit eastward-plunging trends aligned with the regional tectonic framework of the Great Boundary Fault. By integrating both slice and volumetric visualizations within a single figure, the model offers an intuitive and comprehensive perspective of the subsurface, thereby strengthening confidence in the geological interpretation.

Finally, Figure 12 presents depth-wise contour maps from 2 km to 5 km, providing a layered view of density variations at depth and assisting in delineating zones of potential geological significance.

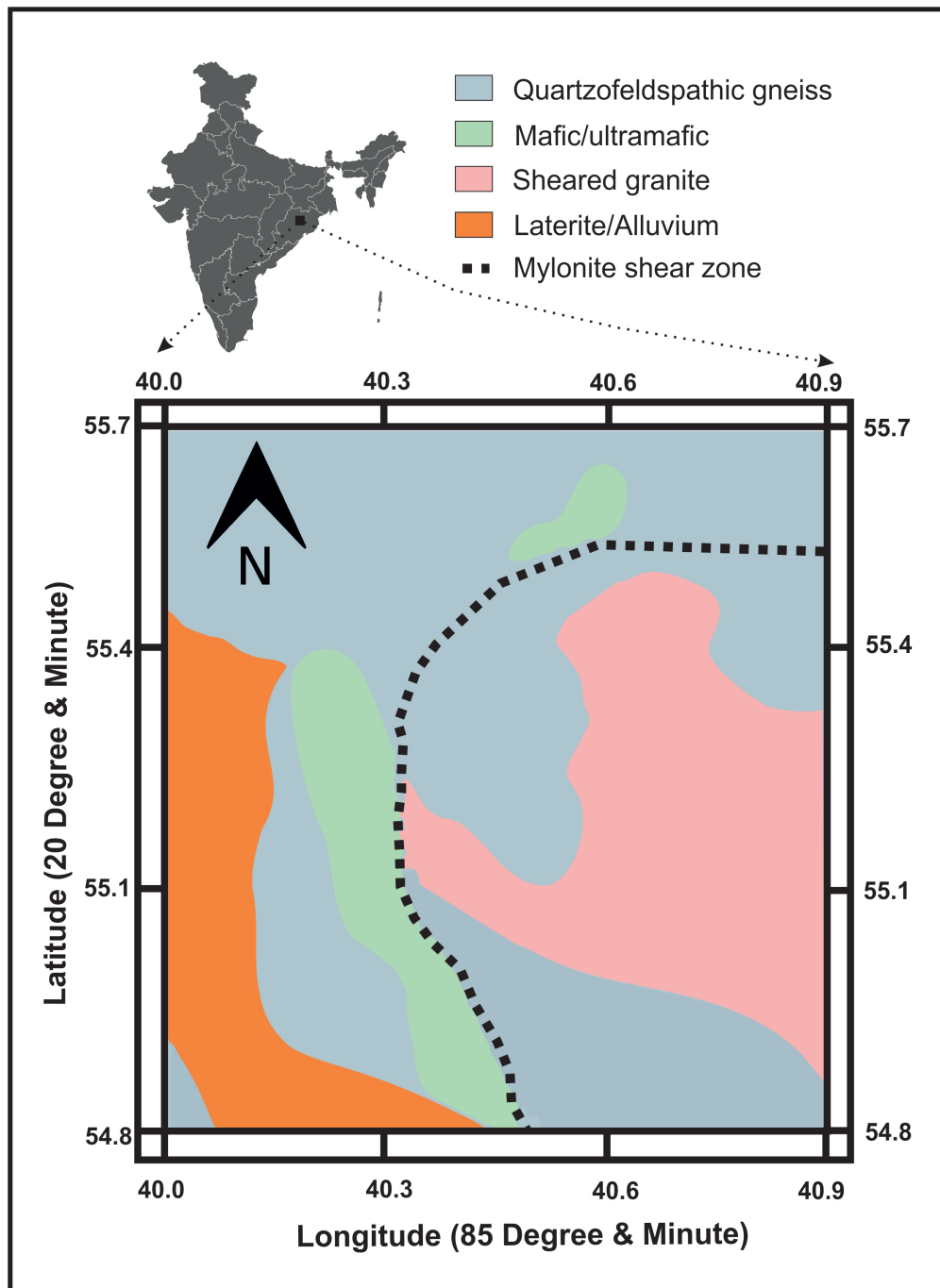


Figure 5: Geological map of the Tangarparha study area, Odisha, India, illustrating the distribution of lithological formations—such as sheared granite, quartzofeldspathic gneiss, and mafic/ultramafic rocks—and key structural features.

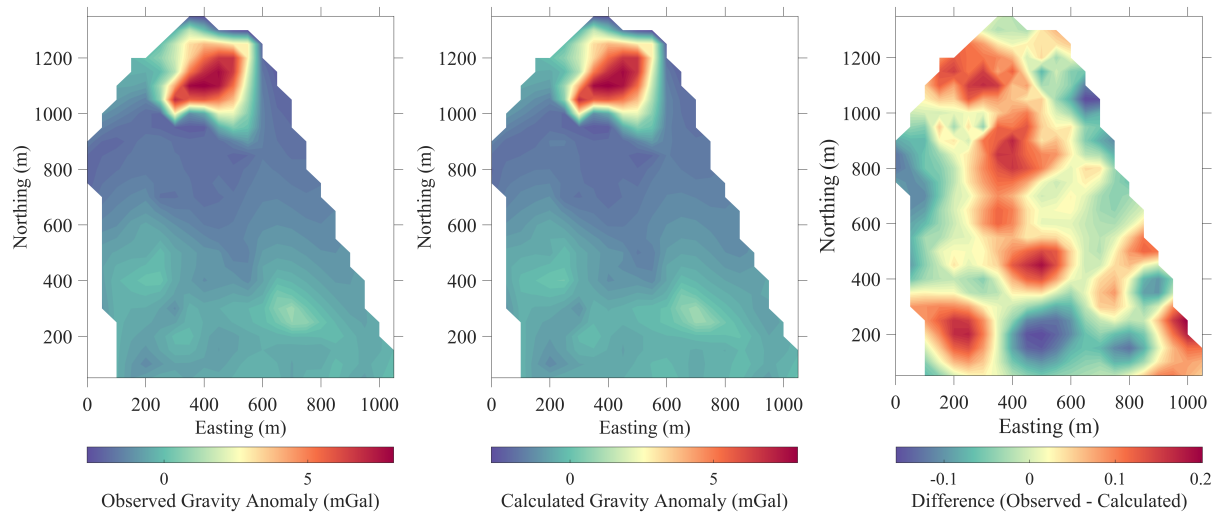


Figure 6: Comparison of residual gravity anomaly maps: observed residual gravity anomaly (left), gravity anomaly calculated from the final 3D inversion model (middle), and the difference map between observed and calculated anomalies (right). The strong similarity in spatial patterns and amplitudes between the observed and calculated fields, together with the low-magnitude residuals, demonstrates the effectiveness of the inversion in resolving subsurface density variations.

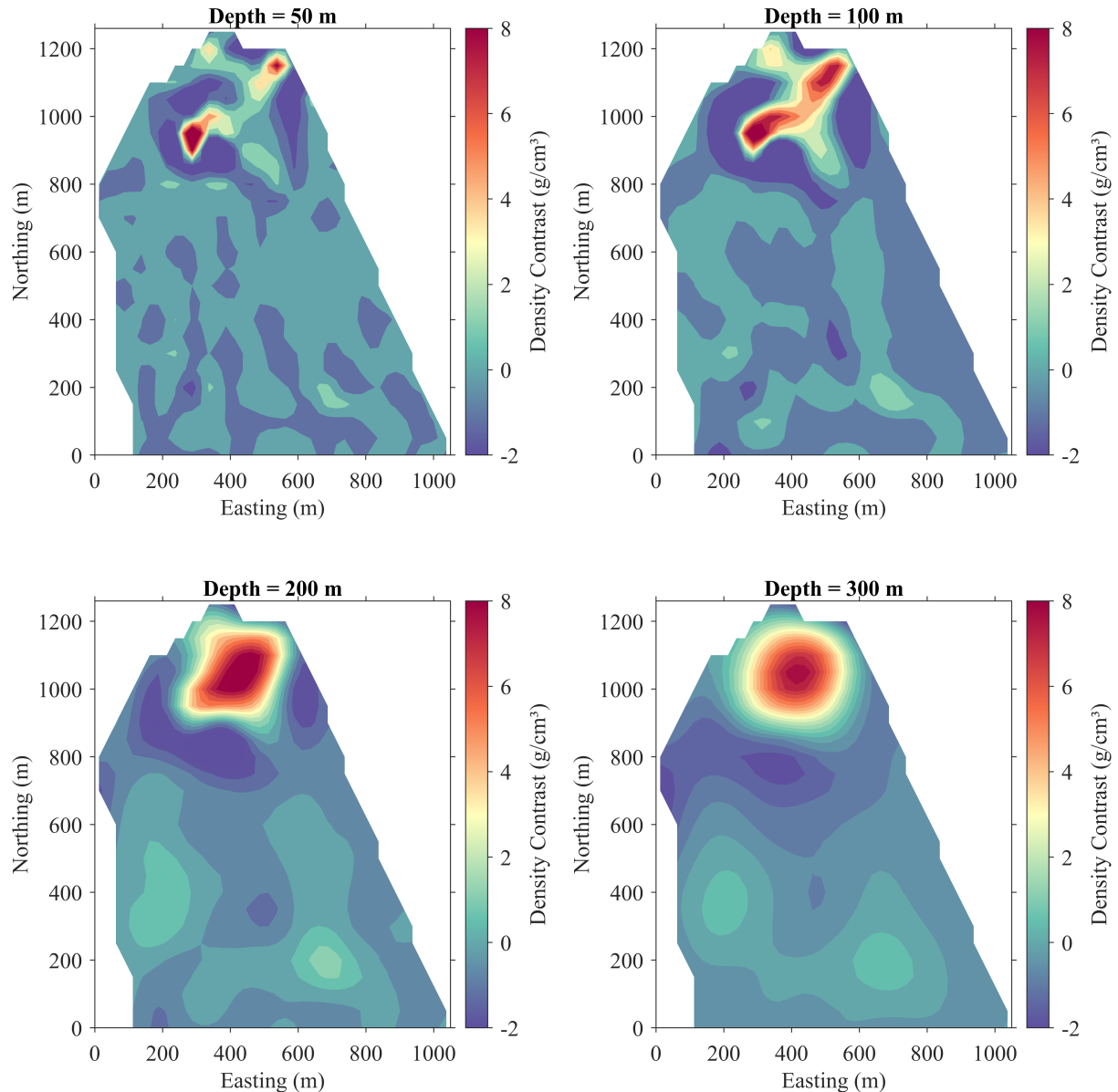


Figure 7: Vertical cross-sections of subsurface density contrast at various depths (50–300 m) from the 3D gravity inversion of the Tangarparha field data. High-density zones suggest mafic/ultramafic intrusions related to chromite mineralization.

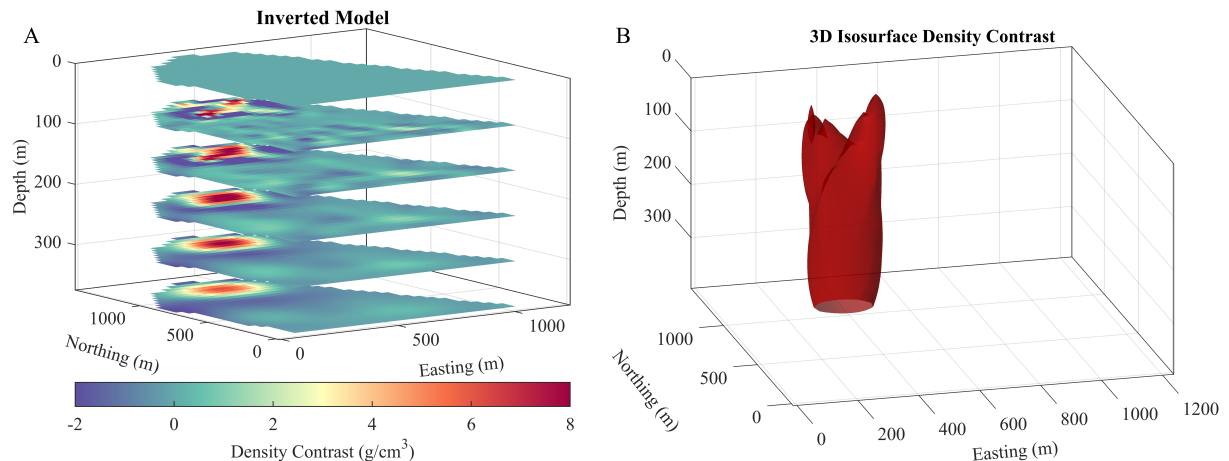


Figure 8: Combined visualization of the 3D inversion results for the Tangarparha study area. The left panel shows the inverted density slice revealing depth-wise density variations and high-density ultramafic zones. The right panel shows the 3D isosurface model, illustrating the geometry and continuity of the dense body responsible for the gravity anomaly.

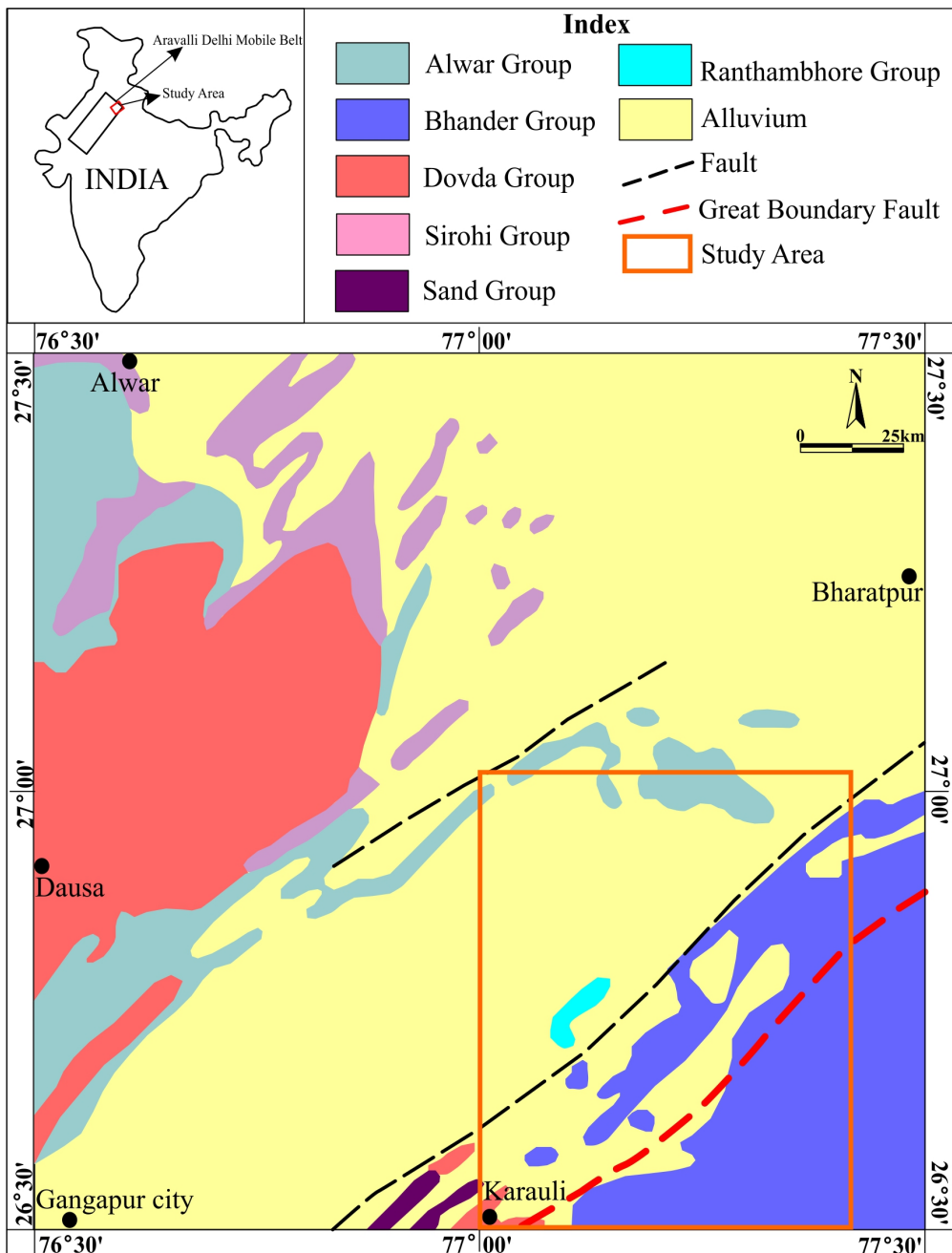


Figure 9: Geological map of the study area located in southeastern Bharatpur District, Rajasthan, India. The map highlights key lithological units, including formations from the Bhander, Alwar, Ranthambhore, Dovda, Sirohi, and Sand Groups, along with Quaternary alluvium. The study area lies along the Great Boundary Fault zone, marking the tectonic transition between the Vindhyan Basin and the Delhi Supergroup. Structural features such as regional faults and the prominent Great Boundary Fault are shown, providing crucial context for interpreting gravity anomalies and subsurface heterogeneity in the region.

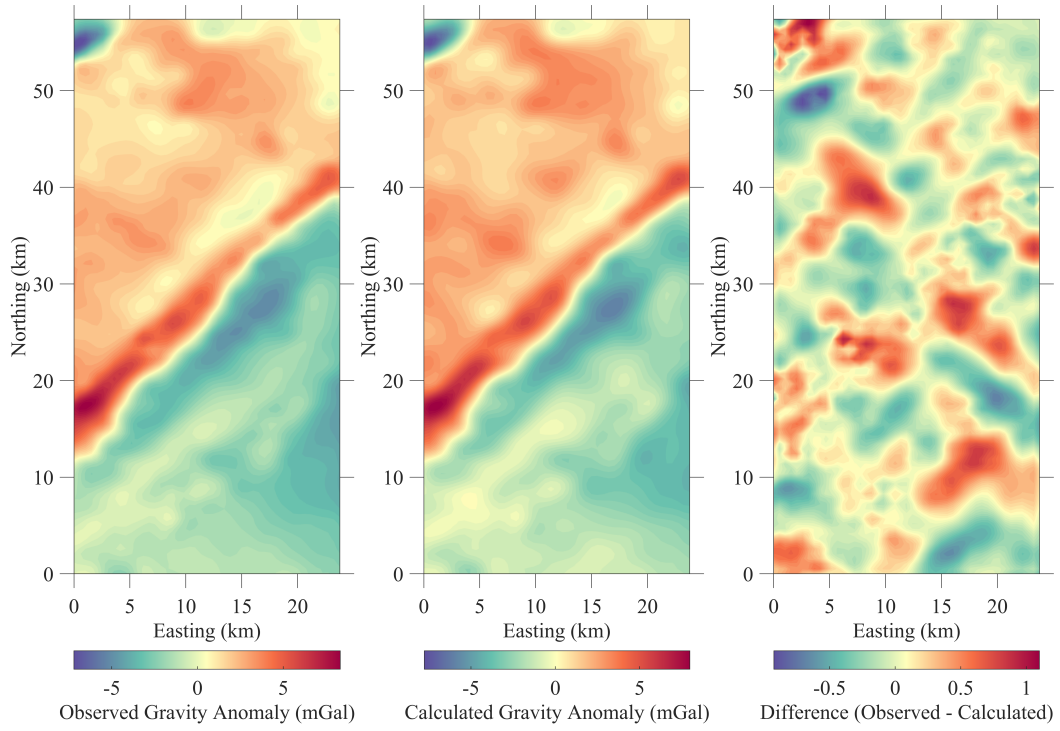


Figure 10: Comparison of residual gravity anomaly maps: observed residual gravity anomaly (left), gravity anomaly calculated from the final 3D inversion model (middle), and the difference map between observed and calculated anomalies (right). The strong similarity in spatial patterns and amplitudes between the observed and calculated fields, together with the low-magnitude residuals, demonstrates the effectiveness of the inversion in resolving subsurface density variations.

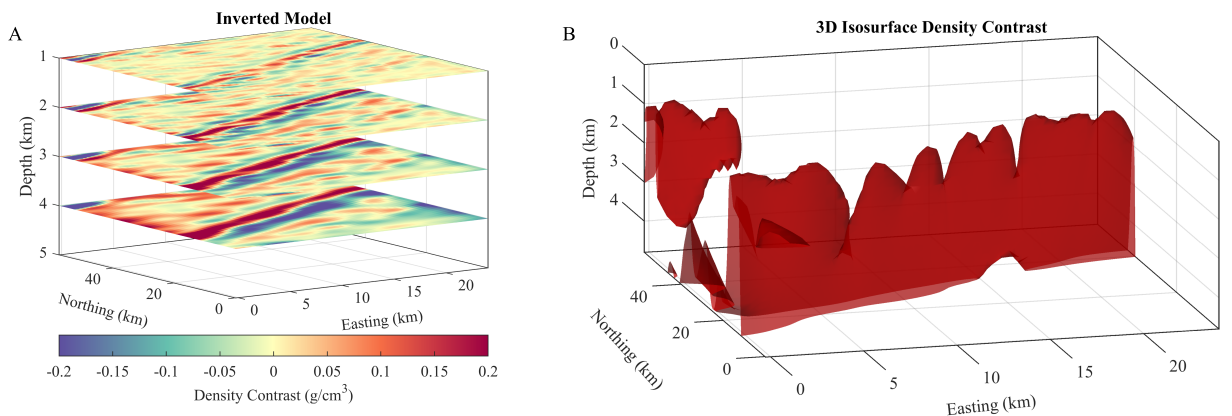


Figure 11: Combined visualization of the 3D gravity inversion model showing (left) vertical slice plots of the recovered density contrast and (right) a 3D isosurface highlighting high-density formations. The slices depict lateral and vertical variations in density, whereas the isosurface reveals the spatial geometry and continuity of dense bodies such as banded iron formations (BIF). Together, they provide a comprehensive understanding of the subsurface structure and its relation to tectonic features associated with the Great Boundary Fault zone.

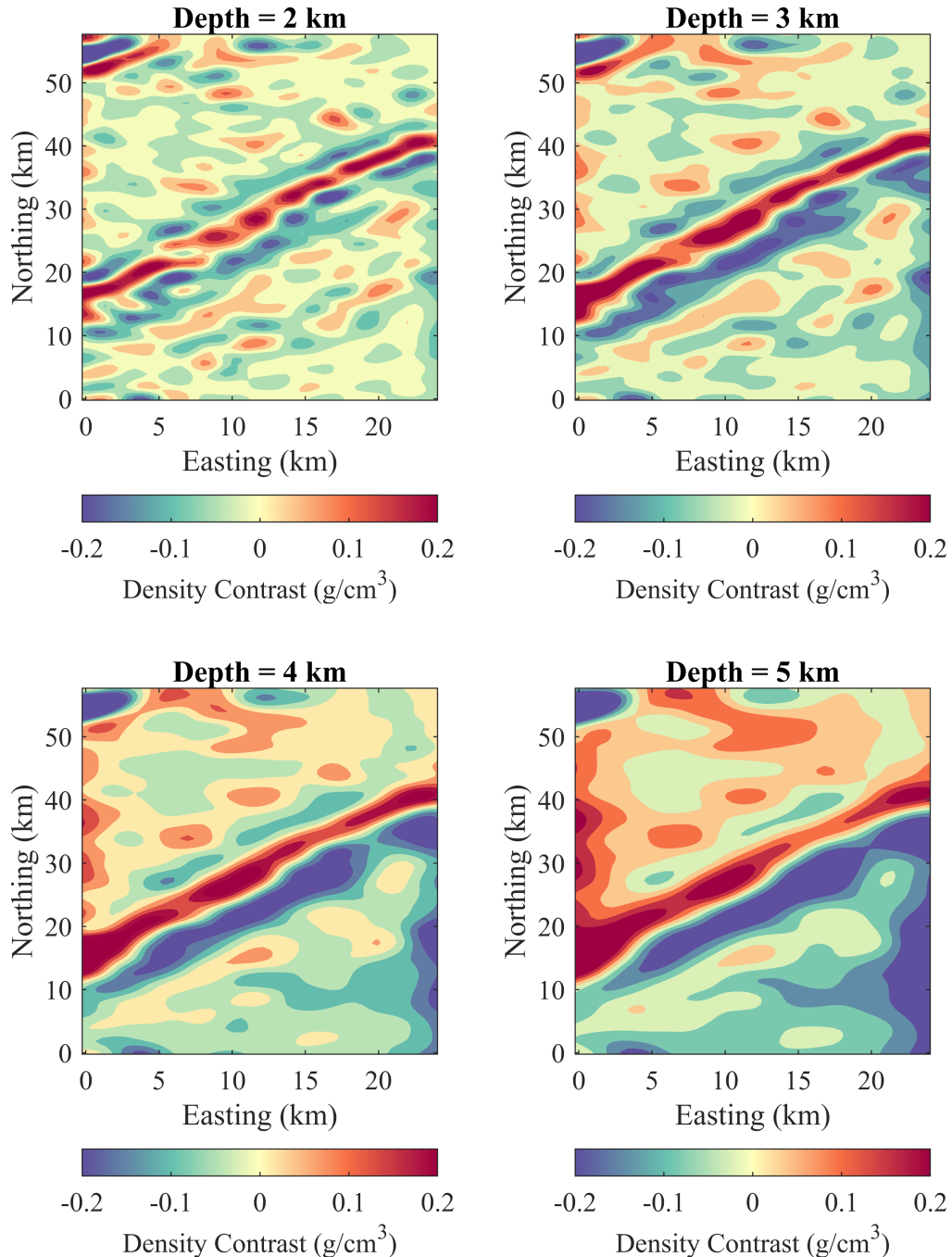


Figure 12: Depth-wise contour maps of subsurface density contrast at 2 km, 3 km, 4 km, and 5 km depth levels derived from 3D gravity inversion. These plots reveal lateral and vertical heterogeneities in the subsurface, highlighting high-density zones interpreted as Banded Iron Formations (BIF) and other dense geological structures. The progressive depth slices aid in visualizing the spatial extent and continuity of subsurface anomalies, supporting tectonic interpretations related to the Great Boundary Fault zone.

5. Conclusion

This study presents a high-performance three-dimensional gravity inversion framework implemented in Julia to address key challenges in geophysical modeling, including computational inefficiency, non-uniqueness, and the ill-posed nature of gravity inversion. By employing a data-space inversion strategy, the framework reduces the dimensionality of the inverse problem, resulting in substantial improvements in computational speed and memory efficiency while preserving inversion accuracy. The incorporation of GPU acceleration further enhances performance, yielding one to two orders of magnitude speedup for large-scale models with up to approximately 3.3 million cells compared to conventional CPU-based implementations. This capability enables practical high-resolution subsurface imaging for applications such as resource exploration and tectonic studies.

The effectiveness of the proposed framework was demonstrated using both synthetic and field datasets. Synthetic experiments showed that the method can reliably reconstruct geometrically complex subsurface structures, including vertical and dipping dykes, while exhibiting expected smoothing near anomaly boundaries due to the inherent non-uniqueness of gravity data. Field applications from Odisha and Rajasthan, India, further confirmed the robustness of the approach, with inversion results showing strong agreement with known geological features such as ultramafic intrusions and banded iron formations. The close correspondence between observed and computed gravity responses highlights the reliability of the framework for real-world gravity inversion problems.

By leveraging Julia's high-performance computing ecosystem and GPU parallelism, the proposed framework overcomes traditional computational bottlenecks associated with large-scale 3D gravity inversion. The scalable and portable design of the implementation makes it well suited for modern high-performance computing environments. Future extensions may include joint inversion with complementary geophysical datasets, such as magnetic or seismic data, to further reduce interpretation uncertainty. Overall, this work provides an efficient and flexible tool for large-scale gravity inversion, with clear potential for both academic research and industrial geophysical applications.

CRediT authorship contribution statement

Nimatullah: Writing – original draft, Writing – review & editing, Software, Methodology, Formal analysis, Data curation, Conceptualization. **Pankaj K. Mishra:** Writing – review & editing, Software, Funding acquisition, Conceptualization, Supervision. **Jochen Kamm:** Writing – Review & editing, Funding acquisition. **Anand Singh:** Writing – review & editing, Software, Funding acquisition, Conceptualization, Supervision.

Software availability

Name of the code/library: GravityInversionGPU.jl: A backend-agnostic Julia framework for three-dimensional gravity modeling and inversion

Contact: Nimatullah (24D0455@iitb.ac.in)

Hardware requirements: GPU acceleration supported (NVIDIA CUDA, Apple Metal, AMD, Intel oneAPI)

Program language: Julia

Software required: Julia (version ≥ 1.9); GPU backend packages (CUDA.jl, Metal.jl, AMDGPU.jl, oneAPI.jl)

Program size: Approximately 0.5 MB (excluding optional dependencies)

Availability of Source Code: The source code is available on Zenodo (<https://doi.org/10.5281/zenodo.18339626>) and GitHub (<https://github.com/naimat04/GravityInversionGPU.jl>).

Acknowledgments

This work was carried out as part of the Ph.D. research of Nimatullah at the Indian Institute of Technology Bombay. The research was financially supported by the Indian Institute of Technology Bombay and the Research Council of Finland under the High-Performance Computing 2023 Project (Grant No. 35926). The authors also acknowledge

the Geological Survey of Finland for institutional support and collaboration. Computational resources and research facilities were provided by CSC – IT Center for Science, Finland, through access to the LUMI supercomputer, and by the Indian Institute of Technology Bombay; both are gratefully acknowledged.

Declaration of generative AI and AI-assisted technologies in the manuscript preparation process

During the preparation of this manuscript, the authors used ChatGPT (OpenAI) and Grammarly to assist with language refinement, improving clarity and readability, and organizing the presentation of the content. The use of these tools was limited to editorial and linguistic support and did not influence the scientific analysis, interpretation of results, or conclusions of the study. All content generated or modified with the assistance of these tools was carefully reviewed, verified, and edited by the authors, who take full responsibility for the accuracy, originality, and integrity of the published work.

References

Bezanson, J., Edelman, A., Karpinski, S., Shah, V.B., 2017. Julia: A fresh approach to numerical computing. *SIAM Review* 59, 65–98. doi:[10.1137/141000671](https://doi.org/10.1137/141000671).

Blakely, R.J., 1996. Potential theory in gravity and magnetic applications. Cambridge University Press.

Bosch, M., McGaughey, J., 2001. Joint inversion of gravity and magnetic data under lithologic constraints. *The Leading Edge* 20, 877–881. doi:[10.1190/1.1487299](https://doi.org/10.1190/1.1487299).

Calcagno, P., Chilès, J., Courrioux, G., Guillen, A., 2008. Geological modelling from field data and geological knowledge. *Physics of the Earth and Planetary Interiors* 171, 147–157. doi:[10.1016/j.pepi.2008.06.013](https://doi.org/10.1016/j.pepi.2008.06.013).

Camacho, A.G., Montesinos, F.G., Vieira, R., 2000. Gravity inversion by means of growing bodies. *Geophysics* 65, 95–101.

Camacho, A.G., Montesinos, F.G., Vieira, R., 2002. A 3-d gravity inversion tool based on exploration of model possibilities. *Computers & Geosciences* 28, 191–204. doi:[10.1016/s0098-3004\(01\)00039-5](https://doi.org/10.1016/s0098-3004(01)00039-5).

Carrillo, J., Gallardo, L.A., 2018. Joint two-dimensional inversion of magnetotelluric and gravity data using correspondence maps. *Geophysical Journal International* 214, 1061–1071. doi:[10.1093/gji/ggy195](https://doi.org/10.1093/gji/ggy195).

Fregoso, E., Gallardo, L.A., 2009. Cross-gradients joint 3d inversion with applications to gravity and magnetic data. *Geophysics* 74, L31–L42. doi:[10.1190/1.3119263](https://doi.org/10.1190/1.3119263).

Gottsmann, J., Camacho, A., Martí, J., Wooller, L., Fernández, J., García, A., Rymer, H., 2008. Shallow structure beneath the central volcanic complex of tenerife from new gravity data: Implications for its evolution and recent reactivation. *Physics of the Earth and Planetary Interiors* 168, 212–230. doi:[10.1016/j.pepi.2008.06.020](https://doi.org/10.1016/j.pepi.2008.06.020).

Hightower, E., Gurnis, M., Van Avendonk, H., 2020. A bayesian 3-d linear gravity inversion for complex density distributions: application to the puysegur subduction system. *Geophysical Journal International* 223, 1899–1918. doi:[10.1093/gji/ggaa425](https://doi.org/10.1093/gji/ggaa425).

Jacoby, W., Smilde, P.L., 2009. Gravity Interpretation: Fundamentals and application of gravity inversion and geological interpretation. Springer. doi:[10.1007/978-3-540-85329-9](https://doi.org/10.1007/978-3-540-85329-9).

Jafarpour, B., Goyal, V.K., McLaughlin, D.B., Freeman, W.T., 2009. Transform-domain sparsity regularization for inverse problems in geosciences. *Geophysics* 74, R69–R83. doi:[10.1190/1.3157250](https://doi.org/10.1190/1.3157250).

Jones, J.P., Okubo, K., Clements, T., Denolle, M.A., 2020. Seisio: A fast, efficient geophysical data architecture for the julia language. *Seismological Research Letters* 91, 2368–2377. doi:[10.1785/0220190295](https://doi.org/10.1785/0220190295).

Lelièvre, P.G., Farquharson, C.G., Hurich, C.A., 2012. Joint inversion of seismic traveltimes and gravity data on unstructured grids with application to mineral exploration. *Geophysics* 77, K1–K15. doi:doi.org/10.1190/geo2011-0154.1.

Li, Y., Oldenburg, D.W., 1998. 3-d inversion of gravity data. *Geophysics* 63, 109–119.

Marchetti, P., Coraggio, F., Gabbiellini, G., Ialongo, S., Fedi, M., 2014. Large-scale 3d gravity data space inversion in hydrocarbon exploration, in: SEG International Exposition and Annual Meeting, SEG. pp. SEG–2014.

Meng, Z., 2018. Three-dimensional potential field data inversion with 10 quasinorm sparse constraints. *Geophysical Prospecting* 66, 626–646. doi:doi.org/10.1111/1365-2478.12591.

Mishra, P.K., 2025. Lithosphere in digital twins of the earth. *Geophysical Journal International* 242, ggaf199. doi:<https://doi.org/10.1093/gji/ggaf199>.

Mishra, P.K., Laaksonen, S., Kamm, J., Singh, A., 2025. Three-dimensional inversion of gravity data using implicit neural representations. URL: <https://arxiv.org/abs/2510.17876>, arXiv:2510.17876.

Mohanty, W.K., Mandal, A., Sharma, S.P., Gupta, S., Misra, S., 2011. Integrated geological and geophysical studies for delineation of chromite deposits: A case study from tangarparha, orissa, india. *Geophysics* 76, B173–B185. doi:[10.1190/geo2010-0255.1](https://doi.org/10.1190/geo2010-0255.1).

Moorkamp, M., Heincke, B., Jegen, M., Roberts, A.W., Hobbs, R.W., 2011. A framework for 3-d joint inversion of mt, gravity and seismic refraction data. *Geophysical Journal International* 184, 477–493. doi:[10.1111/j.1365-246X.2010.04856.x](https://doi.org/10.1111/j.1365-246X.2010.04856.x).

Oldenburg, D.W., Li, Y., 1994. Subspace linear inverse method. *Inverse Problems* 10, 915–935. doi:[10.1088/0266-5611/10/4/011](https://doi.org/10.1088/0266-5611/10/4/011).

Pilkington, M., 2009. 3d magnetic data-space inversion with sparseness constraints. *Geophysics* 74, L7–L15. doi:[10.1190/1.3026538](https://doi.org/10.1190/1.3026538).

Reynolds, J.M., 2011. An introduction to applied and environmental geophysics. Wiley. doi:[10.1071/pvv2011n155other](https://doi.org/10.1071/pvv2011n155other).

Rezaie, M., Moradzadeh, A., Nejati Kalate, A., 2017. 3d gravity data-space inversion with sparseness and bound constraints. *Journal of Mining and Environment* 8, 227–235. doi:doi.org/10.22044/jme.2015.558.

Rim, H., Park, Y., Lim, M., Koo, S.B., Kwon, B.D., 2007. 3d gravity inversion with euler deconvolution as a priori information. *Exploration Geophysics* 38, 44–49. doi:[10.1071/eg07010](https://doi.org/10.1071/eg07010).

Singh, A., 2019. Triangular grid-based fuzzy cross-update inversion of gravity data: Case studies from mineral exploration. *Natural Resources Research* 29, 459–471. doi:[10.1007/s11053-019-09480-x](https://doi.org/10.1007/s11053-019-09480-x).

Tirel, C., Gueydan, F., Tiberi, C., Brun, J., 2004. Aegean crustal thickness inferred from gravity inversion. geodynamical implications. *Earth and Planetary Science Letters* 228, 267–280. doi:[10.1016/j.epsl.2004.10.023](https://doi.org/10.1016/j.epsl.2004.10.023).

Utsugi, M., 2019. 3-d inversion of magnetic data based on the l_1-l_2 norm regularization. *Earth Planets and Space* 71. doi:[10.1186/s40623-019-1052-4](https://doi.org/10.1186/s40623-019-1052-4).

Wang, J., Meng, X., Li, F., 2015. A computationally efficient scheme for the inversion of large scale potential field data: Application to synthetic and real data. *Computers & Geosciences* 85, 102–111. doi:[10.1016/j.cageo.2015.09.005](https://doi.org/10.1016/j.cageo.2015.09.005).